FULL PAPER

Light-to-Heat Conversion

ADVANCED
ENERGY
MATERIALS

www.advenergymat.de

Biomimetic MXene Textures with Enhanced Light-to-Heat Conversion for Solar Steam Generation and Wearable Thermal Management

Kerui Li, Ting-Hsiang Chang, Zhipeng Li, Haitao Yang, Fanfan Fu, Tingting Li, John S. Ho, and Po-Yen Chen*

2D materials are of particular interest in light-to-heat conversion, yet challenges remain in developing a facile method to suppress their light reflection. Herein, inspired by the black scales of *Bitis rhinoceros*, a generalized approach via sequential thermal actuations to construct biomimetic 2D-material nanocoatings, including $Ti_3C_2T_x$ MXene, reduced graphene oxide (rGO), and molybdenum disulfide (MoS_2) is designed. The hierarchical MXene nanocoatings result in broadband light absorption (up to 93.2%), theoretically validated by optical modeling and simulations, and realize improved light-to-heat performance (equilibrium temperature of 65.4 °C under one-sun illumination). With efficient light-to-heat conversion, the bioinspired MXene nanocoatings are next incorporated into solar steam-generation devices and stretchable solar/electric dual-heaters. The MXene steam-generation devices require much lower solar-thermal material loading (0.32 mg cm^{-2}) and still guarantee high steam-generation performance (1.33 kg m^{-2} h^{-1}) compared with other state-of-the-art devices. Additionally, the mechanically deformed MXene structures enable the fabrication of stretchable and wearable heaters dual-powered by sunlight and electricity, which are reversibly stretched and heated above 100 °C. This simple fabrication process with effective utilization of active materials promises its practical application value for multiple solar–thermal technologies.

1. Introduction

Light-to-heat conversion, as a photothermal technology, is derived from harvesting and converting light irradiation (especially for the abundant and sustainable sunlight) into heat as terminal energy. Because of the highly increasing energy needs for economic growth and the emerging environmental concerns regarding fossil fuels in recent years,[1] light-to-heat conversion is of significant interest to society and has become an important technology for generating sustainable thermal energy. Coupled with its operational simplicity and the wide variety of potential materials,[2] it has been intensively applied in many technologies, including water desalination,[3] power plants,[4] actuators,[5] cancer therapy,[6] etc.

To realize efficient light-to-heat conversion, photothermal materials capable of broadband light absorption have been intensively pursued.[7–9] In the past few years, with the fast development of 2D materials with impressive photoelectronic properties, engineering 2D-material nanocoatings for light trapping and absorption has been of particular technological interest.[2,10,11] However, according to the Fresnel equation, 2D-material nanocoatings are limited by moderate broadband light reflection at the air–dielectric interface due to their intrinsic high refractive indices.[12] Therefore, considerable efforts have been made to suppress the light reflection. One approach is to fabricate the microtextures or microarrays of photothermal materials. Yet, the fabrication processes are generally complex and cost-ineffective, resulting in difficulties in scaled-up manufacture for industrial applications.[12,13] Another approach is to construct a porous matrix to improve light-to-heat performance. However, the porous active layers always require high areal loading of 2D materials due to their relatively large thickness (millimeter range) to ensure efficient light absorption, and some fabrication processes are highly energy-consuming (e.g., chemical vapor deposition),[14,15] resulting in high material and manufacturing cost. In addition, the porous matrixes suffer from low mechanical flexibility and nonstretchability, leading to an extremely limited application in steam generation.[16] To promise practical application value of 2D materials for multiple solar–thermal technologies, it is desirable to develop a facile and generalized method for various 2D materials to construct high-performance light-to-heat
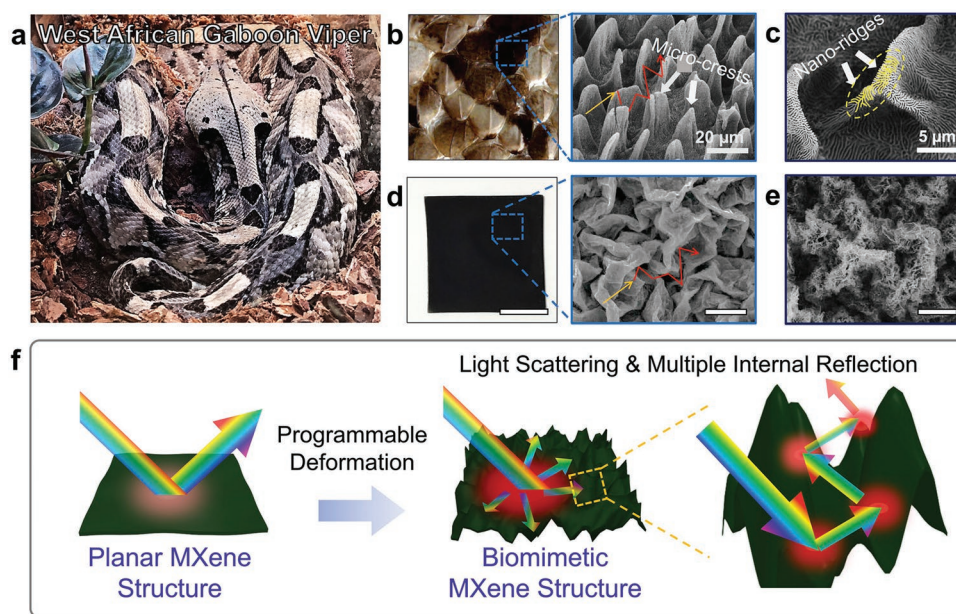
Dr. K. R. Li, Dr. T.-H. Chang, Dr. H. T. Yang, Dr. F. F. Fu, Dr. T. T. Li, Prof. P.-Y. Chen
Department of Chemical and Biomolecular Engineering
National University of Singapore
Singapore 117585, Singapore
E-mail: checp@nus.edu.sg
Dr. Z. P. Li, Prof. J. S. Ho
Department of Electrical and Computer Engineering
National University of Singapore
Singapore 117583, Singapore
Prof. P.-Y. Chen
Department of Chemical and Biomolecular Engineering
University of Maryland
College Park, MD 20742, USA

The ORCID identification number(s) for the author(s) of this article can be found under https://doi.org/10.1002/aenm.201901687.

**ADVANCED
SCIENCE NEWS**

www.advancedsciencenews.com

**ADVANCED
ENERGY
MATERIALS**

www.advenergymat.de

Figure 1. Multigenerational hierarchical MXene structures with broadband light absorption and enhanced light-to-heat performance inspired by the black scale textures of *Bitis rhinoceros*. a) Digital photograph of *Bitis rhinoceros*, the West African Gaboon viper. b) Digital photograph (left) and SEM image (right) of the black dorsal scales of *Bitis rhinoceros*. The surface of the black scales was covered with intensive microcrest structures. c) High-magnitude SEM image of the black scale. Branched nanoridges were present on the microcrest structures. Panels b,c are reproduced with permission.[21] Copyright 2013, Macmillan Publishers Limited. d) Digital photograph (left; scale bar: 1 cm) and SEM image (right; scale bar: 10 μm) of the G_1 MXene nanocoating. e) SEM image of the hierarchical MXene nanocoating (scale bar: 30 μm). f) Schematic illustration of the biomimetic MXene nanocoating with broadband light absorption and enhanced light-to-heat performance.

converters with efficient material utilization and high mechanical stability.

In nature, light exists everywhere, both on the Earth's surface mainly from solar radiation as the energy source of different organisms,[17] and in deep sea from the bioluminescence of some animals.[18] To utilize inexhaustible solar energy efficiently or to meet functional demands for a greater chance of survival, many species were optimized during hundreds of millions of years of natural evolution and developed unique architectures to form darker features to absorb the light.[19–22] For example, besides white hair for camouflage and thermal insulation, polar bears have rough black skin under their white hair to absorb sunlight efficiently and convert it to thermal energy. This light-to-heat skin is crucial to maintaining their internal body temperature at a steady 37 °C in severe cold climate.[20] In addition, West African Gaboon viper (*Bitis rhinoceros*), one kind of ectotherm, features black spots on its dorsal scales with geometrically patterned surface textures (**Figure 1**a,b). The related study by Spinner et al. revealed that the unique hierarchical microstructures that coincide with the distribution of black coloration can impede light reflection and improve the absorption of sunlight.[21] This improved light absorption can warm the black-dot areas to a temperature 2 °C higher than the smoother areas under electrical lamp illumination.

In this work, we mimicked the hierarchical textures of West African Gaboon vipers' black scales and constructed biomimetic nanocoatings in various 2D materials, including titanium carbides ($Ti_3C_2T_x$ MXene), reduced graphene oxide

(rGO), and molybdenum disulfide (MoS_2), through sequential thermal actuations. By undergoing the first-time deformation, the planar MXene nanocoatings were deformed into isotropic crumpled structures, which imitated the microcrest structures of viper's black scales. The incident light was strongly scattered and reflected multiple times within the bioinspired MXene nanocoatings, causing broadband light absorption (84.9–86.9%) and improved equilibrium temperature (58.2–62.6 °C under one-sun illumination) compared with the planar MXene samples (46.8–64.0% and 50.4–58.1 °C). Furthermore, the higher generation MXene nanocoatings were prepared with a hierarchical structure by undergoing second- and third-time deformations. The hierarchical MXene nanocoatings demonstrated further improvements on the light absorption (93.2%) and the light-to-heat performance (up to 65.4 °C). At last, the bioinspired MXene nanocoatings were constructed on two kinds of supporting substrates for thermal insulation and mechanical stretchability to realize high-performance steam-generation devices and stretchable solar/electric heaters, respectively. The steam-generation devices with bioinspired MXene nanocoatings required much lower solar–thermal material loading (0.32 mg cm^{-2}) and still guaranteed high steam-generation performance (1.33 kg m^{-2} h^{-1} under one sun illumination) in comparison with other state-of-the-art devices. Additionally, the mechanically deformed MXene structures enabled the fabrication of wearable and stretchable heaters that were copowered by sunlight and electricity, and heated above 100 °C only under the voltage of 4 V and one-sun illumination.

**ADVANCED
SCIENCE NEWS**
www.advancedsciencenews.com

**ADVANCED
ENERGY
MATERIALS**
www.advenergymat.de

2. Results and Discussion

2.1. Scale Textures of West African Gaboon Viper

The dorsal scales of *Bitis rhinoceros,* a West African Gaboon viper, exhibit alternating colors (in black, light brown, and pale white) and provide effective camouflage for the viper, which lives at the bottom of the forest (Figure 1a). On the black scales, hierarchical structures containing dark pigments were observed. The primary structure consists of many neighboring microcrests with an average height of about 30 µm and a crest-to-crest distance of about 20 µm (Figure 1b). On the surface of primary microcrests, there are intensive nanoridges (Figure 1c). With the hierarchal crest–ridge structures, incident light is highly scattered and internally reflected multiple times within the black scales, resulting in much lower reflectance (10.8%) and higher light absorption (≈84%) than the reflectance (26.7%) and absorption (≈58%) of pale white scales in the visible light spectrum.[21] The higher light absorption finally leads to the profoundly dark appearance of the black scales on West African Gaboon vipers.

2.2. Biomimetic Hierarchical MXene Structures

Inspired by the scale textures of *Bitis rhinoceros*, we constructed similar hierarchical crest-ridge structures to enhance light absorption by using efficient 2D photothermal materials (e.g., $Ti_3C_2T_x$ MXene, rGO, and MoS_2) as building block units. After the deposition of 2D materials, the planar 2D-material nanocoatings were sequentially deformed into higher dimensional architectures (the processes are described in detail in Experimental Section). Here, we first selected the MXene nanosheets to harvest sunlight, since MXene has been recently reported to possess great photothermal characteristics.[2,23] Additionally, MXene nanosheets possess excellent aqueous dispersibility, ease of film deposition, and low environmental toxicity, which are conducive to the large-scale fabrication of solar–thermal devices. The surface hydrophilicity of MXene also promises efficient water spread/supply on the solar steam-generation devices. At last, MXene is highly electrically conductive without undergoing any posttreatment, showing high potential in wearable applications. The MXene nanosheets were prepared by etching $Ti_3Al_2C_2$ MAX crystals in a lithium fluoride (LiF) and hydrochloric acid (HCl) solution followed by ultrasonic exfoliation. The X-ray diffraction patterns (XRD) analysis in Figure S1a of the Supporting Information indicates that $Ti_3Al_2C_2$ MAX crystals were fully transformed into $Ti_3C_2T_x$ MXene after the etching and exfoliation processes.[24] The as-prepared MXene dispersion exhibited an absorption peak around 800 nm (Figure S1b, Supporting Information), which was consistent with the results shown in the literature.[25] Both the scanning electron microscope (SEM) and transmission electron microscope (TEM) images confirmed that as-exfoliated MXene nanosheets exhibited a typical 2D structure (Figure S1c,d, Supporting Information).

The MXene dispersion was next drop-cast or spray-coated onto the thermally responsive polystyrene (PS) substrates (i.e., shrink films). After being a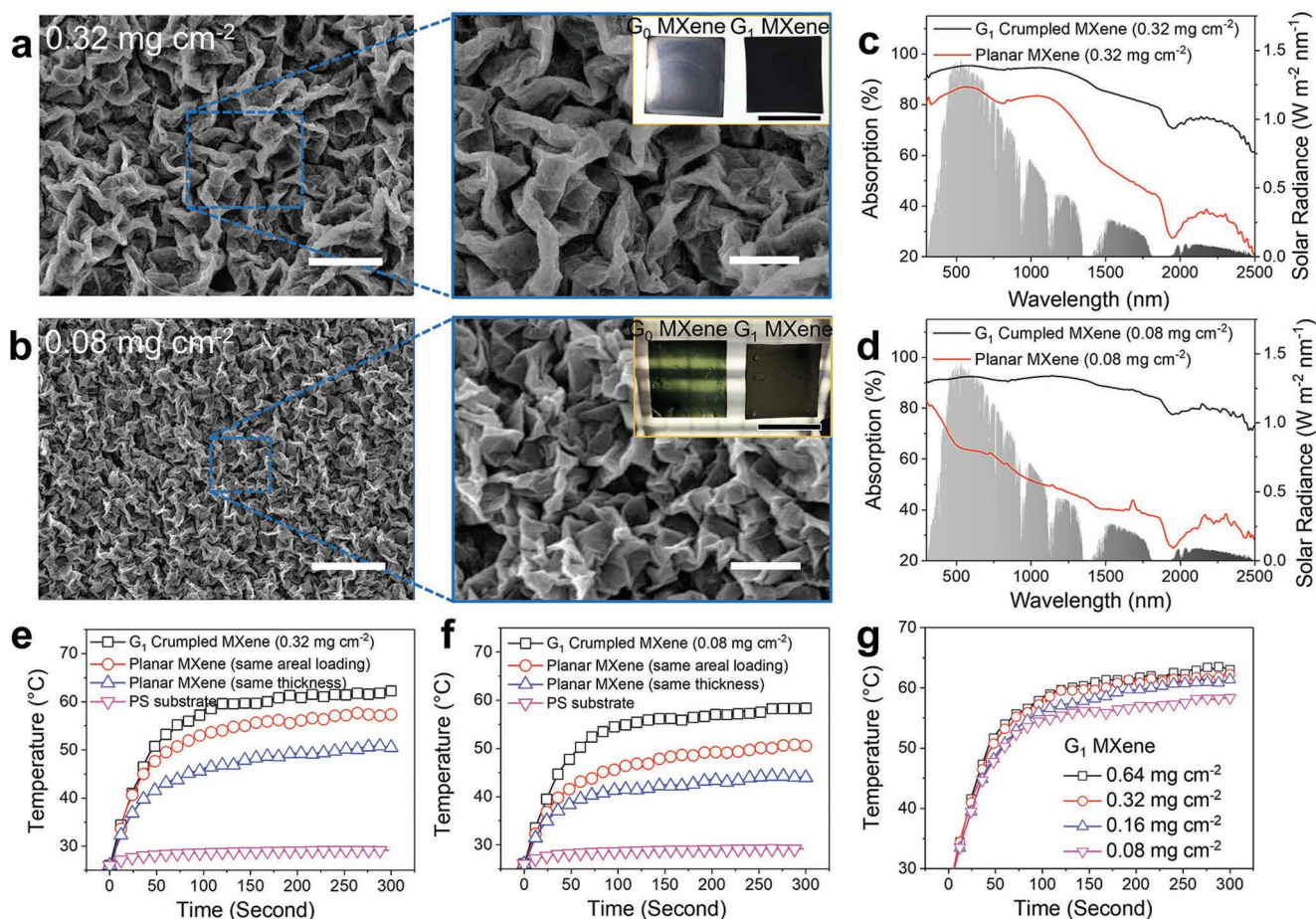ir-dried, the planar MXene samples (denoted as generation 0 (G_0)) were heated above the T_g of PS (≈100 °C),[26] and the G_0 samples were shrunk to ≈50% of the original length and ≈25% of the original area. The biaxial contraction resulted in the deformation of G_0 planar nanocoatings into isotropic crumpled nanocoatings (denoted as G_1, Figure 1d). It should be mentioned that the thermal actuation processes were conducted below 140 °C to avoid the potential oxidation of MXene.[27]

The G_1 nanocoatings further underwent second- and third-round deformations to achieve hierarchical MXene structures. After G_1 shrinkage, the PS substrates were dissolved, and the G_1 MXene nanocoatings were transferred onto new shrink films followed by thermal actuation sequentially. It is worth mentioning that, after the PS substrates were dissolved, the free-standing G_1 MXene nanocoatings left in the solvent were not flattened and still maintained the crumpled structure (Figure S2, Supporting Information). Therefore, by repeating the deformation processes, the higher generation MXene hierarchies (G_2 and G_3) consisting of preserved G_1 structure and newly formed G_2/G_3 structure were obtained with increasing structural complexity. Figure 1e demonstrates the hierarchical G_3 structure with biomimetic crest–ridge features: the primary crumpled structure mimicked the microcrests of vipers' black scales, and the secondary structure (i.e., smaller crumples) was shown on the primary crumples and represented the nanoridge textures. The *Bitis rhinoceros*-inspired MXene structures are expected to induce similar light scattering and internal reflection of incident light within the light-absorbing and light-to-heat hierarchical MXene textures, which can serve as a high-performance solar–thermal system to harvest and convert solar irradiation into thermal energy for various technological applications (Figure 1f).

2.3. G_1 MXene Structures with Broadband Light Absorption

The isotropic crumpled textures can be engineered by the thickness of MXene nanocoatings. As we drop-cast the MXene dispersion on the plasma-treated shrink films at different areal mass loadings from 0.02 to 0.16 mg cm^{-2}, the G_0 planar MXene nanocoatings were obtained with the thickness from ≈71 to 570 nm after being air-dried, respectively (Figure S3a, Supporting Information). The roughness of G_0 planar MXene nanocoatings was also investigated as shown in Figure S3b (Supporting Information). As the areal mass loadings increased, the drop-cast planar MXene nanocoatings became less uniform, and the surface roughness increased accordingly. Such surface nonuniformity and roughness were still smaller than the average thickness of planar MXene nanocoatings, and we found that there was no obvious influence of surface nonuniformity on the ultimate light-to-heat performance after sequential thermal actuations. Meanwhile, we used two other methods, vacuum-filtration and spray-coating (using a U-star airbrush), to improve the surface uniformity of planar MXene nanocoatings (see detailed preparation process and discussion in Figure S3 of the Supporting Information). After the G_1 shrinkage, the G_0 MXene nanocoatings were deformed into isotropic crumpled structures. As the thickness of MXene nanocoatings increased from ≈71 to 570 nm, the peak-to-peak

**ADVANCED
SCIENCE NEWS**
www.advancedsciencenews.com

**ADVANCED
ENERGY
MATERIALS**
www.advenergymat.de

Figure 2. G_1 MXene structures with broadband light absorption and enhanced light-to-heat conversion. SEM images (left, scale bars: 20 μm) and enlarged SEM images (right, scale bars: 10 μm) of G_1 crumpled MXene structures with areal mass loadings of MXene at a) 0.32 mg cm^{-2} and b) 0.08 mg cm^{-2}, respectively. The insets are the photographs of G_0 (planar, left) and G_1 MXene (right) nanocoatings with the same MXene loadings at a) 0.32 mg cm^{-2} and b) 0.08 mg cm^{-2} (scale bars: 2 cm). UV–vis–NIR absorption spectra of G_0 and G_1 MXene nanocoatings with the areal mass loadings at c) 0.32 mg cm^{-2} and d) 0.08 mg cm^{-2}. Surface temperature profiles of G_1 MXene nanocoatings under one-sun illumination with the areal mass loadings at e) 0.32 mg cm^{-2} (thickness: ≈286 nm) and f) 0.08 mg cm^{-2} (thickness: ≈71 nm). As the controls, four G_0 MXene nanocoatings were used with the areal mass loadings at e) 0.32 mg cm^{-2} and f) 0.08 mg cm^{-2} and with the nanocoating thickness at e) ≈286 nm and f) ≈71 mm. g) Surface temperature profiles of G_1 MXene nanocoatings with different areal mass loadings as a function of time under one-sun illumination.

distance of G_1 MXene crumples ($λ$) increased approximately from 1.5 to 12.0 μm, respectively (**Figure 2**a,b and Figure S4 of the Supporting Information). The positive relationship between the peak-to-peak distance of G_1 crumples and the coating thickness can be correlated in Equation (1)[28]

$$λ = 2πh\left(\overline{E}_c / 3\overline{E}_s\right)$$ (1)

Here, h is the coating thickness and the plane-strain elastic modulus $\overline{E}_i = E_i / (1 - v_i^2)$ is given in terms of Young's modulus (E) and Poisson's ratio (v) of the coating (c) or shrink film (s), respectively. Given $v_s = 0.34$, E_s (around 140 °C) ≈ 30 MPa, and $v_c = 0.227$,[28–31] the Young's modulus of MXene films (E_c) can be estimated at 3.7 GPa through Equation (1), which is similar with the result in previous work (≈3.5 GPa).[32]

For the planar thin films, when light reaches the interface of one medium (e.g., MXene) from the air, part of incident light is reflected out of the medium and the other part is refracted into the medium, leading to the absorption or transmission of

incident light. The reflectance (R) can be further estimated by the Fresnel equation under the normal incidence situation (i.e., assuming that the incident angle is 0°) in Equation (2)

$$R = \left(\frac{n_1 - n_2}{n_1 + n_2}\right)^2$$ (2)

Here, n_1 and n_2 represent the refractive indices of media 1 and 2, respectively. Therefore, the reflectance increases as the difference between the two refractive indices increases. For the MXene thin films, the refractive index (n_2) is ≈2 in the visible range and increases to ≈5 in the near-infrared range.[33] Considering that the refractive index of air (n_1) is ≈1, the reflectance values under normal incidence can be calculated to be 11% in the visible range and 45% in the near-infrared range. Consistent experimental results were obtained and are shown in Figure S5a of the Supporting Information, where the reflectance of planar MXene nanocoatings (areal mass loading at 0.32 mg cm^{-2}; thickness at 1.14 μm) was ≈15% in the visible

ADVANCED
SCIENCE NEWS
www.advancedsciencenews.com

ADVANCED
ENERGY
MATERIALS
www.advenergymat.de

range and ≈40% in the near-infrared range. Owing to the high reflectance, the average and solar absorptions of 1.14 µm thick MXene nanocoating were 61.1% and 79.3%, respectively.

In contrast, the bioinspired G_1 MXene structures allow incident light to undergo multiple internal reflections and exhibit decreased reflectance and enhanced light absorption. Here, because the G_0 planar MXene nanocoatings were contracted to ≈25% of the original area after G_1 shrinkage, the areal mass loadings quadrupled accordingly (from 0.02–0.16 mg cm^{-2} for G_0 to 0.08–0.64 mg cm^{-2} for G_1 architectures). Therefore, we compared the G_1 MXene nanocoatings (MXene loading of 0.32 mg cm^{-2} and thickness of ≈286 nm) with two G_0 MXene control samples: one G_0 sample had the same areal mass loading at 0.32 mg cm^{-2} (so the G_0 MXene coating was at ≈1.14 µm thickness and 4-time thicker than G_1 nanocoating), while the other G_0 sample had the same nanocoating thickness at ≈286 nm. With the biomimetic crest structures, the reflectance of G_1 MXene nanocoatings decreased to ≈5.2% in the visible region and to ≈20% in the near-infrared range (Figure S5b, Supporting Information), resulting in improved average (A_{avg}) and solar (A_{solar}) absorptions of 85.2% and 92.8% (Figure 2c), respectively. In comparison, the G_0 MXene samples with the same areal mass loading demonstrated much lower average and solar absorptions (A_{avg}: 61.1%, A_{solar}: 79.3%). From the inset photograph of Figure 2a, the G_1 MXene nanocoating did not show reflected light spots and displayed profoundly black color, also proving that the reflectance of crumpled structures was obviously decreased. Similar increase was shown in the G_1 MXene samples with higher areal mass loading (0.64 mg cm^{-2}) (Figure S6, Supporting Information). Detailed comparison of average and solar absorptions between the G_0 and G_1 MXene nanocoatings with different areal mass loadings are shown in Table S1 (Supporting Information).

We next compared the G_1 nanocoatings with the G_0 nanocoatings with the same thickness at 286 nm. As shown in Figure S5b of the Supporting Information, because of the reduced thickness, light not only got reflected, but also went through the planar MXene nanocoatings with the thickness at 286 nm, leading to moderate light transmittance and reflectance. As a result, in comparison with the G_0 nanocoatings with the same thickness (A_{avg}: 46.8%, A_{solar}: 58.1%), the average and solar absorptions of G_1 MXene nanocoatings significantly increased (A_{avg}: 85.2%, A_{solar}: 92.8%).

Such higher dimensional structures became essential to achieve efficient light absorption when the areal mass loading of light-absorbing materials was very low (e.g., less than 0.1 mg cm^{-2}) or when the thickness of active nanocoatings was very small (e.g., less than 100 nm). The mechanically deformed structures demonstrated increased light absorption through scattering and reflecting incident light multiple times to avoid large light transmission.[34] Here, the G_1 MXene nanocoatings with low areal mass loading at 0.08 mg cm^{-2} (nanocoating thickness at ≈71 nm) were also compared with two G_0 MXene samples with the same areal mass loading (0.08 mg cm^{-2}) and the same nanocoating thickness (≈71 nm). As shown in Figure 2d, even with very low loading of active materials, the G_1 MXene nanocoating showed negligible transmittance (0.6%) and low reflectance (12.5%), leading to high average and solar absorptions of 86.9% and 91.0%, respectively (Figure 2d). In

contrast, as shown in the inset of Figure 2b, substantial light was transmitted and also reflected by the planar MXene nanocoatings with the same areal mass loading at 0.08 mg cm^{-2}. Therefore, the G_0 planar MXene nanocoatings presented 18.1% transmittance and 35.1% reflectance (Figure S5, Supporting Information), leading to low average and solar absorptions of 46.8% and 58.1%, respectively (Figure 2d). In addition, under the same thickness at ≈71 nm, the G_0 MXene nanocoatings showed high transmittance at 47.3%, which resulted in a further lower average and solar absorptions of 33.4% and 33.4%.

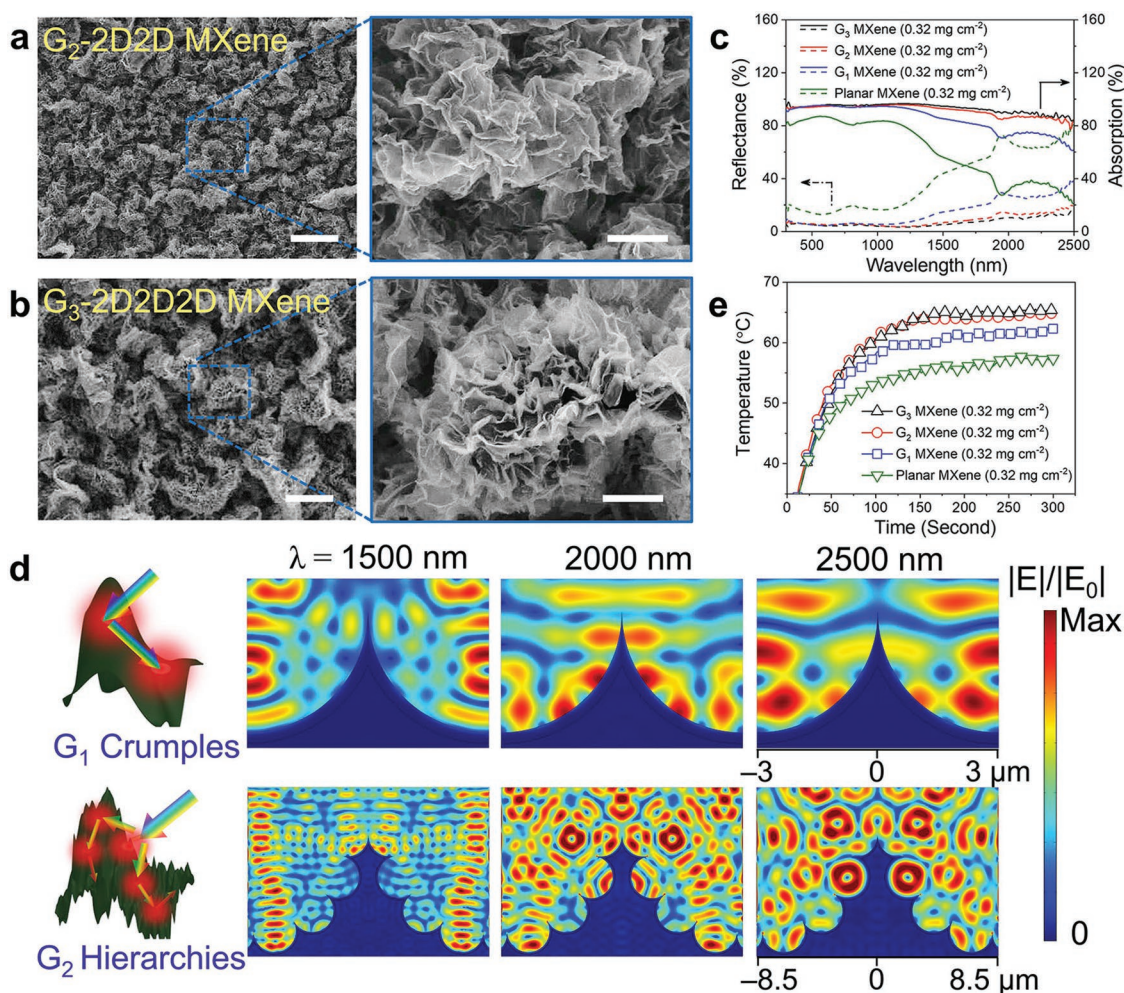## 2.4. G$_1$ MXene Structures with Efficient Light-to-Heat Performance

With increased light absorption, the G_1 MXene nanocoatings exhibited better light-to-heat performance compared with the G_0 planar MXene. We used a solar simulator to simulate one-sun illumination (1.0 kW m^{-2}) and measured the surface temperature of MXene nanocoatings using a thermocouple. The light-to-heat performance can be quantified by the temperature increase ($\Delta T = T_c - T_r$) from the room temperature (T_r) to the surface equilibrium temperature of the MXene nanocoatings (T_c). Figure 2e shows that the G_1 MXene nanocoatings (MXene loading of 0.32 mg cm^{-2} and thickness of ≈286 nm) were heated from 26 to 62.3 °C ($\Delta T = 36.3$ °C) in 5 min. The G_0 MXene samples with the same thickness and the same areal mass loading only showed the temperature increases of 24.4 and 31.4 °C in the same time period, respectively. Similar temperature increase was also demonstrated in the experiment with higher MXene loading (0.64 mg cm^{-2}), where the G_1 MXene nanocoatings were heated from 26 to 62.6 °C ($\Delta T = 36.6$ °C) in comparison with the G_0 MXene samples with the same thickness ($\Delta T = 29.1$ °C).

A larger improvement in light-to-heat performance was observed between the G_1 crumpled and G_0 planar MXene samples with low areal mass loading. As shown in Figure 2f, as the areal mass loading was down to 0.08 mg cm^{-2} and the MXene thickness was at ≈71 nm, the G_1 MXene nanocoatings were still able to be heated from 26 to 58.2 °C ($\Delta T = 32.2$ °C) in 5 min. In contrast, the G_0 MXene samples with the same thickness and the same areal mass loading only showed the temperature increases of 18.0 and 24.4 °C in the same time period, respectively. Moreover, under the same areal mass loadings, the G_1 MXene nanocoatings always showed higher equilibrium temperatures than those of G_0 samples, as expected (Figure 2g; Figure S7a, Supporting Information). Detailed comparison of light-to-heat performance between the G_0 and G_1 MXene nanocoatings with different areal mass loadings are summarized in Table S1 (Supporting Information).

2.5. Higher Generation MXene Structures with Enhanced Light Absorption and Light-to-Heat Performance

To further increase the light absorption and light-to-heat performance, we imitated the hierarchical crest–ridge textures of West African Gaboon vipers' scales and conducted sequential mechanical deformation(s) to achieve hierarchical G_2 or G_3 structures (detailed description is in Experimental Section). As shown in

**ADVANCED
SCIENCE NEWS**
www.advancedsciencenews.com

**ADVANCED
ENERGY
MATERIALS**
www.advenergymat.de

Figure 3. *Bitis rhinoceros*-inspired hierarchical structures with further improved light absorption and light-to-heat performance. a) SEM image (left, scale bar: 50 µm) and enlarged SEM image (right, scale bar: 10 µm) of hierarchical G_2-2D2D MXene structures. b) SEM image (left, scale bar: 50 µm) and enlarged image (right, scale bar: 10 µm) of hierarchical G_3-2D2D2D MXene structures. c) UV–vis–NIR absorption spectra of the MXene nanocoatings at different generations from G_0 (planar) to G_3. All the MXene nanocoatings are with the same mass areal loading. d) Simulated electric field distributions of G_1 (top) and G_2 (bottom) MXene structures at wavelengths (λ) of 1500, 2000, and 2500 nm. e) Surface temperature profiles of different-generation MXene nanocoatings as a function of time under one-sun illumination.

Figure 3a, the repeated 2D contractions (G_2-2D2D) resulted in a much denser crumpled topography with the preservation of G_1 crumples (≈ 3 µm $\times 3$ µm) and reformation of larger feature sizes (≈ 17 µm $\times 17$ µm). The third iteration of mechanical deformation (G_3-2D2D2D) resulted in additional variations, and the multiscale G_3 structures in Figure 3b displayed larger topographical features (G_3 crumples at 30 µm $\times$ 30 µm) decorated with smaller features generated from the previous deformations (smaller G_1, G_2 crumples from less than 1 µm $\times$ 1 µm to more than 5 µm $\times$ 5 µm). The multigenerational MXene nanocoatings demonstrate similar hierarchical structure to the texture of *Bitis rhinoceros'* black scales with both the primary microcrest structures and secondary nanoridge textures, promising further increase in light absorption via the biomimetic technique.

We first characterized the broadband absorption of higher generation MXene nanocoatings by using a UV–vis–NIR spectrometer (Figure 3c). With the crest–ridge hierarchical structures, the reflectance was reduced from 39.4% for G_0 to 14.4% for G_1,

8.3% for G_2, and finally to 6.5% for G_3. Therefore, the average absorption increased from 61.1% for G_0 to 85.2% for G_1, 91.4% for G_2, and 93.2% for G_3, corresponding to the improvement of solar absorption from 79.3% for G_0 to 92.8% for G_1, to 94.1% for G_2, and to 95.1% for G_3. The light absorption of the G_3 MXene nanocoating (93.2%) is higher than that of the viper's black scales (89%)[19] and comparable with those of state-of-the-art microstructural nanocoatings (from 85% to 99%) processed with complex fabrication procedures or high-cost active materials (e.g., Au or Pt).[10,13,35–37] Detailed comparison of optical properties and light-to-heat performance between different-generation MXene nanocoatings are summarized in Table S2 (Supporting Information).

2.6. Optical Modeling and Simulation

To theoretically probe the light absorption mechanism of the hierarchical MXene structures, we performed optical

simulations using commercial software COMSOL Multiphysics based on finite element method (FEM) for the different-generation MXene structures. For simplicity, the crest-like G_1 MXene structure was modeled as a sharp peak spliced by two 90° arcs. For the G_2 hierarchical MXene structure, crest-like primary structure and ridge-like secondary structure were simplified as the larger sharp peak decorated with smaller peaks assembled by the semicircles with the diameter of 3 µm (Figure S7b, Supporting Information). Figure S7c of the Supporting Information shows the simulated absorption spectra of the G_0, G_1, and G_2 MXene nanocoatings, respectively. The G_0 planar MXene demonstrated efficient light absorption in the visible range, yet showed significant decrease in the absorption in the near-infrared range, which was coherent to the calculated results according to the Fresnel equation and measured spectra by UV–vis–NIR spectrometer. In contrast, the light absorption of G_1 structure increased remarkably in the NIR region, and as the G_2 hierarchical structure was formed, further increase in light absorption was observed, which was similar as the experimental results. Figure 3d and Figure S7d of the Supporting Information represent the simulated electric-field (E-field) profiles ($|E|/|E_0|$) of different-generation MXene structures at three NIR wavelengths of 1500, 2000, and 2500 nm. Compared with G_0 MXene structure, the electric field maps of higher generation MXene structures show widely spread hot spots around the MXene structures, indicating field confinement induced by strong localized surface plasmon resonances at near-infrared frequencies.[37] Through the theoretical and experimental analysis, the broadband light absorption can be concluded as follows. When incident light reaches the hierarchical MXene structure, the multiscale structures with nanoscale to microscale crumples induce strong light scattering and multiple internal reflection, resulting in strong reflection suppression. In addition, the light fields are confined on the surface of MXene structures by the localized surface plasmon resonance, and then convert to thermal energy by Ohmic loss of MXene structures,[38] leading to low light transmission, and thus broadband light absorption and heat generation.

The light-to-heat performances of high-generation MXene nanocoatings are shown in Figure 3e. With further enhanced solar absorptions over 90%, the G_2 and G_3 MXene nanocoatings under one-sun irradiation were heated from 26 °C to higher equilibrium temperatures of 64.8 and 65.4 °C in 5 min. Because of slight increase in the solar absorption from G_2 to G_3, the equilibrium temperatures of the two nanocoatings were almost the same. Nevertheless, the highest temperature of 65.4 °C is still striking considering that the mass loading of photothermal material is as low as 2 mg on a 2.5 × 2.5 cm^2 substrate (0.32 mg cm^{-2}).

2.7. A Generalized Approach to Achieving Biomimetic Hierarchical Structures of 2D Materials Beyond MXene

Besides MXene, the sequential mechanical deformations provide a generalized approach to fabricating the biomimetic crest–ridge structures in various 2D materials, including rGO and MoS$_2$. We were able to design different solar–thermal devices according to the physicochemical properties of 2D materials (e.g., environmental stability, surface hydrophilicity/hydrophobicity, bandgap, etc.). Moreover, with a wide selection for 2D materials, the photothermal performance can be further optimized according to practical operating conditions. For example, as we described above, Ti$_3$C$_2$T$_x$ MXene nanosheets show many advantages, including excellent aqueous dispersibility, ease of film deposition, low environmental toxicity, surface hydrophilicity for efficient water spread/supply, etc. One of the technological limits of MXene is the tendency of oxidization. Therefore, the MXene-based devices may need to be operated at a lower temperature (no more than 100 °C) or be encapsulated in oxygen/moisture barriers for long-term operation. Compared with MXene, rGO exhibits great environmental stability even at high temperatures and under long-term operation. Yet, the intrinsic hydrophobicity of rGO layer may be a disadvantage for water spread/supply when the dimension of steam-generation devices becomes large. What is more, many semiconducting nanomaterials (especially with narrow bandgaps) were used for light-to-heat conversion. Therefore, we used MoS$_2$ as the representative for the fabrication of solar–thermal devices. The unique bandgap structures can provide potential applications in multifunctional photoelectric devices through the integration of light-to-heat feature with other photoelectric properties of semiconducting 2D materials.

The preparation of MoS$_2$ nanosheet dispersion was described in Experimental Section. The morphology of MoS$_2$ nanosheets was characterized by TEM and exhibited a typical 2D structure (Figure S8a, Supporting Information). The XRD spectrum of MoS$_2$ multilayered film revealed two characteristic peaks (Figure S8b, Supporting Information), which is consistent with the results in the literature.[39] The G_1 rGO and MoS$_2$ nanocoatings were produced through the same thermal actuation process (the details are in Experimental Section). Similar to the MXene case, as the areal mass loadings increased from 0.08 to 0.32 mg cm^{-2}, the peak-to-peak distances increased approximately from 2.0 to 10.0 µm for the G_1 rGO case and from 1.5 to 8.0 µm for the G_1 MoS$_2$ case (Figures S9 and S10, Supporting Information). As expected, the G_1 rGO and MoS$_2$ nanocoatings also showed improved internal reflection and higher light absorption in comparison with the G_0 samples. As shown in Figure S11 and summarized in Table S1 of the Supporting Information, all the G_1 nanocoatings demonstrated >14% increase in the average absorption and >11% increase in the solar absorption over the G_0 nanocoatings under the same areal mass loadings. Because of higher percentage solar absorption under one-sun illumination, the surface temperatures of G_1 nanocoatings (at 0.32 mg cm^{-2}) increased from 26 to 62.8 °C (rGO) and 58.6 °C (MoS$_2$), while the G_0 rGO and MoS$_2$ nanocoatings were heated to 58.9 °C and 53.2 °C, respectively (Figure S12, Supporting Information).

The biomimetic crest–ridge hierarchies in rGO and MoS$_2$ were also achieved by performing repeated 2D contraction (i.e., G_2 deformation) to improve light absorption further. As shown in Figure S13 of the Supporting Information, the G_2 rGO and MoS$_2$ nanocoatings displayed similar hierarchical structures with preserved G_1 secondary crumples and reformed G_2 primary crumples. As expected, with the hierarchical textures, the light-to-heat performances of G_2 hierarchical structures were improved (Figure S14, Supporting Information), and the G_2
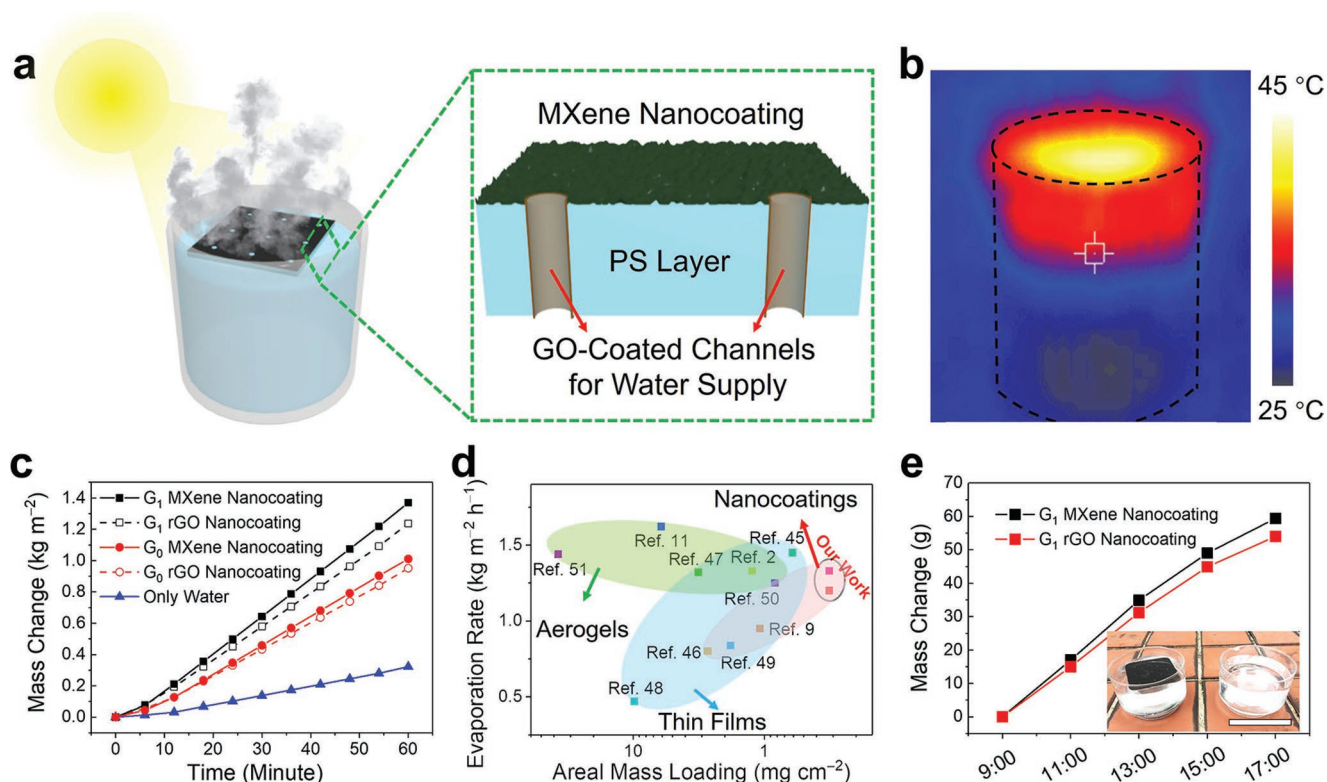
Figure 4. Bioinspired G_1 MXene structures with enhanced solar–thermal conversion for efficient solar steam generation. a) Schematic illustration of the solar steam-generation device with the bioinspired MXene nanocoating for high solar–thermal conversion. b) Infrared image demonstrates the temperature distribution of the steam-generation device floating on the water bath in a beaker after 30 min one-sun illumination at 1.0 kW m⁻². The black dashed lines represent the approximate edges of the beaker. c) Mass changes of water over time for different solar–thermal conversion layers under one-sun illumination. Above experiments were conducted at the ambient temperature of ≈26 °C and the humidity of ≈55%. d) Comparison in terms of the areal mass loadings of active materials and the evaporation rates between our steam-generation devices and the reported steam-generation devices in the literature. e) Outdoor steam-generation performance for scaled-up MXene and rGO devices on a sunny day. The inset digital photograph is the setup for outdoor steam generation (scale bar: 10 cm).

rGO and MoS_2 nanocoatings under the areal mass loading at 0.32 mg cm⁻² were able to be heated to 64.9 °C (rGO) and to 60.2 °C (MoS_2).

Based on the mechanically deformed microstructure with broadband light absorption and light-to-heat performance, we further constructed the higher dimensional nanocoatings of 2D materials on two different substrates, a thermal insulation layer to realize the solar steam-generation devices, and a latex substrate to demonstrate the stretchable dual-powered MXene heaters for wearable thermal management, in order to show the multifunctionality of biomimetic structures.

2.8. Bioinspired MXene Nanocoatings as Solar–Thermal Conversion Layers for Efficient Steam Generation

Solar steam generation is emerging as one of the promising solar energy technologies, and the potential applications involve water desalination, purification, distillation, sterilization, etc.[40–42] Solar steam generation has been increasingly developed in recent years via two approaches of improving the energy conversion efficiency and minimizing the energy losses.[43] Yet, challenges still remain in applying the steam-generation devices to cost-effective industrial applications,

which require the breakthroughs in reducing material and fabrication cost, simplifying processing methods, and guaranteeing high conversion efficiency. The outstanding light absorption and light-to-heat performance of bioinspired 2D-material nanocoatings (e.g., G_1 MXene) provide a promising approach to developing efficient solar steam-generation devices with cost-effective utilization of active materials.

The solar steam-generation devices were designed as illustrated in **Figure 4**a and shown in Figure S15 (Supporting Information). We first fabricated the G_1 MXene nanocoating (as a solar–thermal conversion layer) on a 1.5 mm thick PS supporting substrate (as a thermal insulator). Then, multiple small channels (≈1.5 mm in diameter) were drilled in the MXene/PS bilayer device, and the cylindrical surface of channels was coated with a hydrophilic GO layer for water supply. The device was finally floated on the water surface and acted as a localized solar–thermal converter.

Under solar radiation, the G_1 MXene layer was heated and started to evaporate water on its surface. Because of the thermal insulation of the PS substrate, when the temperature of the upper water reached around 45 °C, the temperatures at other positions slightly changed (Figure 4b). We also used the thermocouple to validate the temperatures at different water levels. After one-sun illumination for 30 min, the water near the

steam-generation device was locally heated from 26 to 45 °C, but the temperature of water beneath the steam-generation device at a 6 cm depth remained around 29 °C. The configuration of MXene/PS bilayer device enabled the localized heating at the interface of water and PS substrate, largely preventing energy loss to bulk water.

We further evaluated the performance of solar steam generation by measuring the water evaporation rates. As shown in Figure 4c, the G_1 MXene steam-generation devices showed an evaporation rate of 1.37 kg m^{-2} h^{-1} under one-sun illumination, which was higher than those of the G_0 planar MXene device with the same areal mass loading (1.01 kg m^{-2} h^{-1}) and pure water (0.32 kg m^{-2} h^{-1}) (Table S3, Supporting Information). G_1 rGO conversion layers were also constructed to extend the material types for steam-generation devices and demonstrated an evaporation rate of 1.24 kg m^{-2} h^{-1}, which was higher than the G_0 rGO layer (0.95 kg m^{-2} h^{-1}).

The solar energy conversion efficiency (η) is another important parameter in solar steam generation, and the efficiency can be calculated via Equation (3)

$$\eta = \dot{m} \times h_{LV} / q_i \times C_{opt} \tag{3}$$

where $\dot{m}$ is the net evaporation rate calculated by subtracting the evaporation rates under the dark condition from the measured evaporation rates (Table S3, Supporting Information), h_{LV} is the liquid–vapor phase enthalpy change, including sensible heat (79.8 J g^{-1}, from ≈26 to 45 °C with a specific heat of 4.2 J g^{-1} K^{-1} and) and phase change enthalpy (2383 J g^{-1} at 46 °C), q_i is the nominal solar illumination of 1.0 kW m^{-2}, and C_{opt} is the optical concentration. The conversion efficiencies of the G_1 MXene and rGO devices were calculated to be 90.1% and 82.1%. These values are comparable with the state-of-the-art results in previously reported work.[16,44,45] Generally, to reach high evaporation rates, high areal mass loading of active materials (more than 1 mg cm^{-2} in most of the literature) were required to ensure efficient light absorption and solar–thermal conversion, which may result in high material cost and thus limit the applications from large-area devices. In comparison, our steam-generation devices based on the biomimetic MXene nanocoatings required lower areal mass loading of active materials (0.32 mg cm^{-2}) and still guaranteed high steam-generation performance compared with most of the state-of-the-art steam-generation devices reported previously (Figure 4d; Table S3, Supporting Information),[2,9,11,45–51] showing high competitiveness in industrial applications.

Besides the advantage of a lower amount of active materials used, the thermally responsive deformation approach is scalable to achieve large-area bioinspired nanocoatings for fabricating steam-generation devices, which is urgently required at industrial level. As shown in the inset of Figure 4e, we utilized the doctor-blading method to fabricate the large-area G_1 2D-material nanocoatings at ≈60 cm^2 (see detailed description in Experimental Section). It is worth noting that the device size can be further scaled-up if there is a larger thermally responsive PS substrate available. To demonstrate practical use of the G_1 2D-material converter, large-area steam-generation devices with G_1 nanocoatings were placed on water surface and illuminated under natural solar light. As shown in

Figure 4e, 60 cm^2 sized MXene and rGO devices generated 17.9 g (i.e., 8.95 g h^{-1}) and 16.2 g (i.e., 8.1 g h^{-1}) of steam, respectively, under the sunlight illumination for 2 h on a sunny day, and produced 59.4 g and 54.0 g of steam, respectively, from 9 a.m. to 5 p.m. on a sunny day (temperature: ≈30 °C; humidity: ≈75%). In contrast, without the crumpled active layer, only 25.1 g of steam was produced under the same operating conditions.

The antifouling issue (especially for salts) should be considered for the practical operation of steam-generation devices in seawater.[52] Here, we tested the solar steam-generation performance of our G_1 MXene devices in simulated seawater (an aqueous solution of NaCl with 3.5 wt%). As shown in Figure S16a of the Supporting Information, under one-sun illumination, the evaporation rate of G_1 MXene devices was almost invariable during the first 1 h, and gradually decreased by 10.3% after 2 h operation caused by the accumulation of salt crystals on the MXene nanocoating (Figure S16b, Supporting Information). Although the evaporation rate did not decay obviously during 3 h, the antifouling issue should be considered carefully and pursued to address in our future work.

2.9. Highly Stretchable MXene Nanocoatings via Reversible Crumpling/Unfolding Processes

Besides efficient solar steam generation, the higher dimensional MXene nanocoatings can undergo reversible crumpling and unfolding, endowing high mechanical stretchability to MXene for wearable applications. We transferred a planar MXene film onto a prestretched elastomeric substrate (e.g., inflated latex balloon or prestretched VHB tape) followed by the biaxial contraction. The strong adhesion of MXene nanocoatings on elastic substrate was facilitated by oxygen plasma treatment and incorporation on GO adhesion layer (see detailed fabrication process in Experimental Section). After the elastic substrate was gradually relaxed, the transferred MXene film was biaxially compressed into out-of-plane microcrumples. As the areal strain was applied from 0% to 800% by re-inflating the latex balloon from 0 to 150 cm^3 again, the G_1 MXene nanocoatings were biaxially expanded (**Figure 5**a). The expansion of G_1 MXene nanocoatings led to the unfolding of microcrumples and increased the peak-to-peak distance from ≈5 to 40 μm (Figure 5b). Upon the release of biaxial strain, the G_1 MXene structures were recovered. During the biaxially crumpling/unfolding processes, the resistance of G_1 MXene nanocoatings was monitored and showed excellent cycling stability (Figure S17, Supporting Information), further proving the structural integrity and excellent stretchability of G_1 MXene nanocoatings. Interestingly, with the reversible crumpling/unfolding processes, the reflectance was controlled from 15.2 to 33.4% under the applied areal strain from 0% to 800% due to the gradually flattening and reinstating of the microstructure (Figure S18, Supporting Information). The strain engineering in the MXene microstructure and its tunable optical properties may lead to potential applications in the fields of optical sensing and dynamic camouflage.
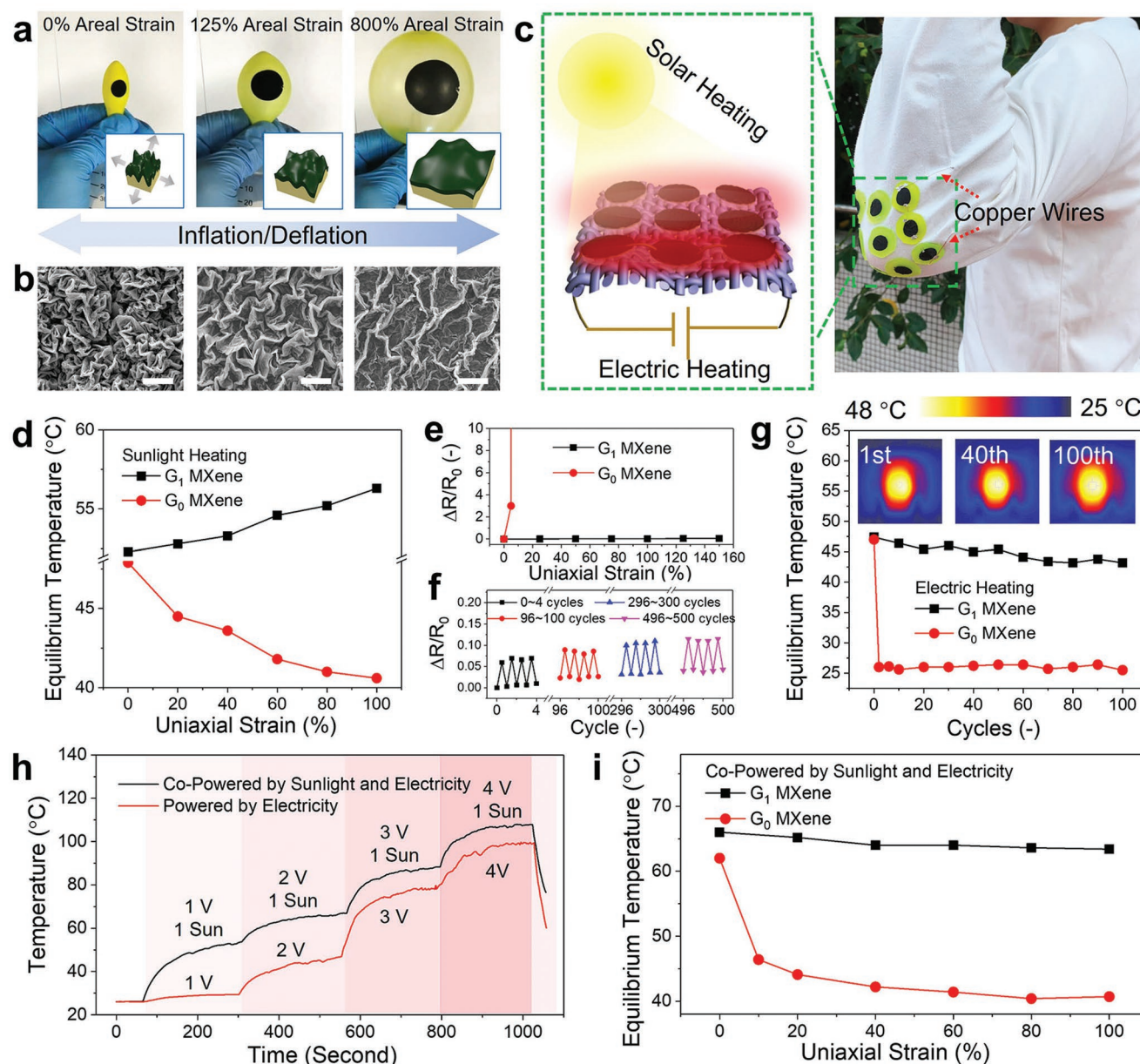
Figure 5. G_1 MXene nanocoatings with large mechanical deformability for stretchable solar/electric dual-heaters. a) Digital photographs and b) SEM images (scale bars: 20 µm) of the G_1 MXene nanocoating on a latex balloon at different biaxial stretching states. The inset schemes represent the structural change of G_1 MXene nanocoating at different stretching states. c) Schematic illustration (left) and digital photograph (right) demonstrate that the stretchable solar/electric MXene heaters were integrated on a T-shirt for wearable thermal management. d) Equilibrium temperatures of G_1 and G_0 MXene heaters under one-sun illumination at different uniaxial strains. Relative resistance changes of the stretchable MXene heaters e) under different uniaxial strains and f) during repeated uniaxial stretching/relaxation cycles. g) Equilibrium temperatures of the G_1 and G_0 MXene heaters powered by a voltage at 2 V at repeated stretching/relaxation cycles. The insets are infrared images of the stretchable MXene heater at different cycles. h) Surface temperature profiles of stretchable solar/electric MXene heaters copowered by one-sun illumination and different voltages. i) Equilibrium temperatures of stretchable solar/electric MXene heaters under different uniaxial strains.

2.10. Highly Stretchable MXene Nanocoatings for Wearable Solar/Electric Dual-Heaters

The demands for wearable or even skin-mountable heaters have been increasing due to their applications in personal heating systems and healthcare management.[53–55] Current wearable heaters are mainly electrically driven and suffer from

the needs of constant and steady energy supply. For comfortable wearing experience as well as low and safe driving voltages, challenges remain in the development of wearable heaters that are mechanically deformable and can be dual-powered by other green and sustainable energy resources. The G_1 MXene nanocoatings on elastic substrates can be utilized as the stretchable electrodes for wearable heaters that can be self-powered by

**ADVANCED
SCIENCE NEWS**

www.advancedsciencenews.com

**ADVANCED
ENERGY
MATERIALS**

www.advenergymat.de

solar illumination and heated on demand by an applied voltage (illustrated in Figure 5c).

We first measured the light-to-heat performance of stretchable MXene heater under different uniaxial strains after one-sun illumination for 5 min. As shown in Figure S19 of the Supporting Information, the stretchable MXene heater was quickly heated from 26 to ≈55 °C under all applied uniaxial strains. The stretchable MXene heater demonstrated a slightly increased equilibrium temperature from 52 to 56 °C as the uniaxial strains increased from 0% to 100% (Figure 5d), due to the preservation of microstructures and the increased active area for receiving more sunlight under stretching. In contrast, the planar MXene heater was broken under 10% stretching and formed large cracks/fractures (Figure S20a, Supporting Information), and these cracks/fractures led to thermal diffusion and loss to low-temperature fractured areas and eventually lower equilibrium temperature.

Furthermore, because of the high electrical conductivity of MXene (≈2000 S cm^{-1} in this work), the G_1 MXene nanocoating was utilized as a stretchable resistive heater. The stretchable resistive heaters highly relied on the strain-independent resistance profile of G_1 MXene nanocoatings. As shown in Figure S20b of the Supporting Information, the morphology was first characterized during a stretching process and showed high mechanical stability without the generation of microfractures. The G_1 MXene nanocoating only showed a 6.0% increase in film resistance under a large uniaxial strain (150%), leading to a small gauge factor of ≈0.04 (Figure 5e). We further measured the resistance changes in a stretching/relaxation cycling test under a maximum uniaxial strain of 100%. As shown in Figure 5f, the film resistance stayed nearly unchanged (<5.0%) after 500 cycles. Under an applied voltage (2 V), the stretchable MXene heater was heated to ≈47.5 °C and maintained an equilibrium temperature of 43.2 °C after 100 stretching/releasing cycles (Figure 5g; Figure S18c, Supporting Information), demonstrating a mechanically stable MXene resistive heater for wearable thermal management. In contrast, the planar MXene nanocoatings were fractured obviously under a small strain of 10% and demonstrated irreversible resistance increase. Therefore, the surface temperature of the planar MXene heater quickly decreased to room temperature at about 26 °C once a 20% strain was applied (Figure S18d, Supporting Information).

Because the G_1 MXene nanocoatings exhibited strain-stable solar/electric heating performance, the stretchable dual-powered MXene heaters were achieved. As shown in Figure 5h, the surface temperature of a stretchable MXene heater was manipulated by both solar illumination and applied voltages, and the equilibrium temperatures were ramped up to 107.7 °C under one-sun illumination and 4 V. At lower voltages (1 V and 2 V) and under one-sun illumination, the stretchable MXene heater was heated quickly to 52.7 and 66.9 °C in 240 s, respectively, meeting the requirement of personal thermal management in low energy consumption and safety. In contrast, if merely powered by the voltage at 1 V and 2 V (without sunlight), the stretchable MXene heater was only heated to 29.4 and 44.6 °C, respectively. More importantly, as shown in Figure 5i, the dual-powered MXene heater exhibited great mechanical stability under large uniaxial strains up to 100% (over the maximum tolerant strains of human skin),[56] and maintained 90% of original equilibrium temperature after 100 uniaxial stretching/relaxation cycles (Figure S21a, Supporting Information). The stability of dual-powered MXene heaters was also characterized by measuring the surface temperature under 2 V voltage and one-sun illumination for 10 h. As shown in Figure S21b of the Supporting Information, the surface temperature of the dual-powered MXene heater decreased only from 66.3 to 59.9 °C. Furthermore, to improve the stability of MXene heaters, we intentionally spin-coated a transparent, elastic, and thin polydimethylsiloxane (PDMS) layer on the MXene surface to prevent the contact with oxygen/moisture.[57] With the protective PDMS coating, the dual-powered MXene heater demonstrated improved stability with the temperature decrease from 66.6 to 63.7 °C after 10 h testing, which is consistent with the resistance changes (Figure S21c, Supporting Information). These G_1 MXene nanocoatings provide a promising material choice for the fabrication of stretchable dual-powered heaters for wearable technologies with superior heating performance, self-power solar–thermal options, low energy consumption, and low-voltage safety.

3. Conclusion

In summary, inspired by the hierarchical crest-ridge scale texture of *Bitis rhinoceros*, we designed a simple and generalized method to harness the interfacial instability for constructing crumpled textures and further forming higher generation hierarchical nanocoatings in various 2D materials (from MXene to rGO and MoS$_2$). With multiple light scattering and trapping induced by the multiscale textures, the biomimetic 2D-material nanocoatings enabled broadband light absorption and finally led to increased light-to-heat performance under one-sun illumination. The higher generation (G_2, G_3) hierarchical MXene structures showed higher solar absorption (up to 95%) and higher equilibrium temperature (65.4 °C), presenting better light trapping and thermal management than the performances of *Bitis rhinoceros*.

Besides the fundamental discussion on broadband light absorption and light-to-heat performance, we fabricated two kinds of devices with the bioinspired 2D material nanocoatings to present the multifunctionality of our approach in many fields. First, through transferring the bioinspired MXene nanocoating onto a thermal insulation substrate, we achieved a high-performance steam-generation device with a high conversion efficiency of 86.7%. Moreover, the steam-generation device was scaled-up to a large-area module and showed practical application in natural sunlight. Next, as the bioinspired MXene nanocoatings were supported by elastic substrates, we were able to reversibly unfold and reinstate the crumpled structures to achieve a stretchable solar/electric dual-heater for wearable thermal management. We envision that the surface processing technology has extremely practical application value in multiple solar–thermal fields by simply harnessing interfacial instability to construct the biomimetic hierarchical structures in various nanomaterials.

4. Experimental Section

Materials: GO aqueous dispersion (Angstron Materials Incorporation, 5 mg mL^{-1}), bulk MoS$_2$ powders (Sigma-Aldrich), and Ti$_3$AlC$_2$ (MAX,

Tongrun Info Technology Co., Ltd, China) powders were used as received without further purification. Clear polystyrene (PS) heat shrink films were purchased from Grafix. DI water (18.2 MΩ) was used as the water source throughout the work and obtained from a Milli-Q water purification system (Millipore Corp., Bedford, MA, USA).

Preparation of $Ti_3C_2T_x$ MXene Nanosheets: $Ti_3C_2T_x$ MXene nanosheets were prepared according to the literature with slight modification.[24] 4.0 g of LiF and 2.0 g of Ti_3AlC_2 MAX were slowly added to 9.0 M HCl solution (40 mL) under vigorous stirring. The mixture was kept at 35 °C for 24 h. After that, the solid residue was washed successively with 2.0 M HCl solution and DI water for several times until the pH value was above 5.0. Subsequently, the washed residue was added into 100 mL of DI water, ultrasonicated for 2 h under N_2, and centrifuged at 3000 r.p.m. for 20 min. The supernatant was collected as the final suspension of $Ti_3C_2T_x$ MXene nanosheets.

Preparation of MoS_2 Nanosheets: MoS_2 nanosheets were exfoliated by Li-ion intercalation into bulk MoS_2 crystals as reported previously.[58] 0.3 g of MoS_2 powders was added into 3 mL of n-butyllithium solution (Sigma-Aldrich) under argon atmosphere and stirred for 5 d. The mixture was then centrifuged and washed with hexane to remove the excess of butyllithium. The Li-ion-intercalated MoS_2 was dispersed in water and sonicated for 1 h, and the obtained MoS_2 dispersion were centrifuged at 5000 r.p.m. for 30 min to separate unexfoliated materials. At last, the supernatant was dialyzed to remove residual Li ions. As-synthesized MoS_2 nanosheets were the mixed 2H/1T phase.[39,59]

Fabrication of Multigenerational Structures for 2D Materials: PS shrink film was cut into 5 cm × 5 cm squares and washed with DI water and ethanol successively. The substrates were treated with air plasma in a Harrick plasma cleaner for 4 min. This pretreatment of the PS substrate with oxygen plasma can increase hydrophilic interactions and hydrogen bonding with 2D materials.[60] Then, the MXene, GO, or MoS_2 solution was drop-coated on the plasma-treated shrink films. After being air-dried, the planar nanocoating (we called it G_0) was obtained, and the samples were placed in an oven at 140 °C (above the T_g of PS (≈100 °C)) for 6 min. Afterward, the samples were removed from the oven and allowed to cool down to obtain G_1 2D-material samples with shrunk area of ≈2.5 cm × 2.5 cm (we called it G_1). Here, the G_1 GO samples were immersed into a hydroiodic acid/acetic acid (volume ratio of 1:1) mixed solution for 12 h to obtain rGO samples. To achieve hierarchical MXene nanocoatings, the PS substrates were dissolved in dichloromethane (DCM), and the G_1 MXene structures were left in the solvent. The free-standing MXene films were sequentially rinsed with DCM for twice to remove the residual PS and finally with ethanol. The freestanding MXene films were transferred to new plasma-treated shrink films, and G_2 hierarchies were obtained after G_2 shrinkage. After repeating the same processes (dissolving the substrates, washing, transferring, G_3 shrinkage), we can obtain the multiscale G_3 films. It is worth mentioning that, to maintain the same MXene loading at 0.32 mg cm^{-2} (i.e., 2 mg of MXene on 2.5 cm × 2.5 cm of substrate) in the G_2 and G_3 nanocoatings, the starting G_0 nanocoatings (2 mg of MXene) were prepared on 9 cm × 9 cm and 16 cm × 16 cm of shrink films, respectively. Therefore, the thicknesses of original G_0 nanocoatings for the G_2 and G_3 structures were about 13 and 40 times smaller than the planar control samples.

Fabrication of Solar Steam-Generation Devices: MXene dispersion was first drop-coated on a PS film. After the thermal shrinkage process, the G_1 MXene nanocoating (with areal mass loading of 0.32 mg cm^{-2}) was constructed as a solar–thermal conversion layer. Meanwhile, the PS layer became thicker (with thickness of 1.5 mm) due to the thermal shrinkage and was utilized as supporting substrate and thermal insulator directly. Small water channels (≈1.5 mm in diameter) were then drilled in the MXene/PS bilayer device with the channel-to-channel spacing around 1.5 cm. GO dispersion was injected into the channels using a syringe. After being air-dried at room temperature, hydrophilic GO layers were coated on the cylindrical surface of channels for water supply. Large-area steam-generation devices were prepared based on the G_1 rGO active layer. First, the GO dispersion (5 mg mL^{-1}) was centrifuged at 10 000 r.p.m. for 20 min. The precipitated GO was collected, stirred, and sonicated to obtain the concentrated GO slurry (12 mg mL^{-1}). Then,

10 mL of GO slurry was doctor-bladed onto a 240 cm^2 sized plasma-treated shrink film by using a home-made equipment. After thermal shrinkage, the large-area G_1 GO nanocoating (≈60 cm^2) was constructed on the PS supporting substrate. Finally, the GO nanocoating was reduced in a hydroiodic acid/acetic mixed solution to obtain the large-area steam-generation device.

Fabrication of Highly Stretchable MXene Heaters: 4 mL of diluted GO dispersion (0.05 mg mL^{-1}) was first filtrated onto a circular filtration membrane with a 3.6 cm diameter (Merck Millipore, 0.22 μm pore size). Successively, 16 mL of MXene dispersion (0.05 mg mL^{-1}) was filtrated onto the GO layer to form a MXene/GO bilayer composite. After being dried at room temperature, the MXene/GO film on the filtration membrane was immersed into ethanol, and then was easily peeled off in ethanol to form a free-standing film. At this process, the GO layer was used as a mechanical protective layer to avoid the fracture of MXene layer caused by the swelling of the polyvinylidene difluoride (PVDF) filtration membrane. A latex balloon was then treated with air plasma for 4 min to form oxygenated groups on the surface, which were able to increase the hydrophilic interactions and hydrogen bonding with the GO protective layer.[60] The free-standing MXene/GO film was carefully transferred onto the plasma-treated inflated latex balloon. The expansion degrees of substrate can be controlled by the amount of water or air. After being dried at room temperature, the latex balloon was then slowly deflated, and the MXene/GO nanocoating was deformed into G_1 crumpled structures.

Optical Modeling and Simulation: The simulation results were carried out using commercial software COMSOL Multiphysics based on finite element method by frequency domain. The boundary conditions of the simulation region were set as periodic for the x-directions. The broadband plane wave from 300 to 2500 nm was incident to the structure with electric field along the x-axis. The scattering parameters S_{11} and S_{21} were obtained from the software and the optical absorption was calculated by equation $1 - S_{11}^2 - S_{21}^2$. For simplicity, we assumed that distribution of the microcrumples is homogeneous with same peak-to-peak distance and geometry (discussed above). The thicknesses of G_0, G_1, and G_2 MXene nanocoatings were set as same as those of the corresponding experimental samples with the MXene loadings at 0.32 mg cm^{-2} (i.e., 1140, 284, and 71 nm for G_0, G_1, and G_2 MXene nanocoatings, respectively). The permittivity of MXene were referred to the previous work.[37]

Characterization and Measurements: XRD patterns were measured using an X-ray diffractometer (Bruker, D8 Advance X-ray Powder Diffractometer, Cu Kα (λ = 0.154 nm) radiation) at a scan rate of 4° min^{-1}. The morphologies of different 2D nanosheets and their stacked films were characterized by using a SEM (FEI Quanta 600), a field emission scanning electron microscope (FESEM, JEOL-JSM-6610LV) operating at 15.0 kV for high-resolution imaging, and a high-resolution transmission electron microscopy (HRTEM, JEOL 2010F). The thickness and roughness profiles of MXene nanocoatings were measured using a surface profiler (Alpha-Step IQ). A solar beam was generated from a solar simulator (Newport 91195A) with the power density of 1.0 kW m^{-2}. The surface temperatures before and after solar illumination were measured using a thermocouple thermometer (TC-08, Picotech, UK) and the temperature distribution was measured using an IR camera (HT-02, XINTEST, China). Optical measurements were carried out on a UV–vis–NIR Spectrometer (UV-3600, Shimadzu, Japan) with an integrated sphere for reflected light collection. The absorption was then calculated by $A = 1 - R - T$, R and T are the reflectance and transmittance of the sample, respectively. The reflectance (R) was calculated according to the following equation

$$R = \frac{\int R d\lambda}{\Delta\lambda} \tag{4}$$

The average absorption (A_{avg}) was calculated according to the following equation

$$A_{avg} = \frac{\int A d\lambda}{\Delta\lambda} \tag{5}$$

The solar absorption (A_{solar}) was calculated by the following equation[61]

$$A_{solar} = \frac{\int A \times S \, d\lambda}{\int S \, d\lambda} \tag{6}$$

where A is the solar absorption, R is the reflectance of the sample, S is solar spectral irradiance (W m^{-2} nm^{-1}), λ is the wavelength (nm).

The areal strain applied via a biaxial stretching was calculated according to the following equation

$$\text{Areal Strain} = \frac{A_S - A_0}{A_0} \times 100\% \tag{7}$$

where A_0 is area of the G_1 MXene nanocoating on a latex substrate without stretching, and A_s is area of the G_1 MXene nanocoating at the biaxial stretching state.

The uniaxial strain applied on stretchable MXene heaters was defined as follows

$$\text{Uniaxial Strain} = \frac{L_S - L_0}{L_0} \times 100\% \tag{8}$$

where L_0 is the original length of the MXene heater, and L_s is the length of the MXene heater at the uniaxial stretching state.

Supporting Information

Supporting Information is available from the Wiley Online Library or from the author.

Conflict of Interest

The authors declare no conflict of interest.

[1] L. Zhu, M. Gao, C. K. N. Peh, G. W. Ho, *Mater. Horiz.* **2018**, *5*, 323.
[2] R. Li, L. Zhang, L. Shi, P. Wang, *ACS Nano* **2017**, *11*, 3752.
[3] G. Ni, G. Li, S. V. Boriskina, H. Li, W. Yang, T. Zhang, G. Chen, *Nat. Energy* **2016**, *1*, 16126.
[4] M. K. Gupta, S. C. Kaushik, *Renewable Energy* **2010**, *35*, 1228.
[5] J. Mu, C. Hou, H. Wang, Y. Li, Q. Zhang, M. Zhu, *Sci. Adv.* **2015**, *1*, e1500533.
[6] J. Shao, H. Xie, H. Huang, Z. Li, Z. Sun, Y. Xu, Q. Xiao, X.-F. Yu, Y. Zhao, H. Zhang, H. Wang, P. K. Chu, *Nat. Commun.* **2016**, *7*, 12967.
[7] Y. Liu, S. Yu, R. Feng, A. Bernard, Y. Liu, Y. Zhang, H. Duan, W. Shang, P. Tao, C. Song, T. Deng, *Adv. Mater.* **2015**, *27*, 2768.
[8] H. Ghasemi, G. Ni, A. M. Marconnet, J. Loomis, S. Yerci, N. Miljkovic, G. Chen, *Nat. Commun.* **2014**, *5*, 4449.
[9] C. Chen, Y. Li, J. Song, Z. Yang, Y. Kuang, E. Hitz, C. Jia, A. Gong, F. Jiang, J. Y. Zhu, B. Yang, J. Xie, L. Hu, *Adv. Mater.* **2017**, *29*, 1701756.
[10] J. V. Anguita, M. Ahmad, S. Haq, J. Allam, S. R. P. Silva, *Sci. Adv.* **2016**, *2*, e1501238.
[11] X. Hu, W. Xu, L. Zhou, Y. Tan, Y. Wang, S. Zhu, J. Zhu, *Adv. Mater.* **2017**, *29*, 1604031.
[12] Z.-P. Yang, L. Ci, J. A. Bur, S.-Y. Lin, P. M. Ajayan, *Nano Lett.* **2008**, *8*, 446.
[13] K. Bae, G. Kang, S. K. Cho, W. Park, K. Kim, W. J. Padilla, *Nat. Commun.* **2015**, *6*, 10103.
[14] Y. Ito, Y. Tanabe, J. Han, T. Fujita, K. Tanigaki, M. Chen, *Adv. Mater.* **2015**, *27*, 4302.
[15] H. Ren, M. Tang, B. Guan, K. Wang, J. Yang, F. Wang, M. Wang, J. Shan, Z. Chen, D. Wei, H. Peng, Z. Liu, *Adv. Mater.* **2017**, *29*, 1702590.
[16] N. Xu, X. Hu, W. Xu, X. Li, L. Zhou, S. Zhu, J. Zhu, *Adv. Mater.* **2017**, *29*, 1606762.
[17] D. Stuart-Fox, E. Newton, S. Clusella-Trullas, *Philos. Trans. R. Soc., B* **2017**, *372*, 20160345.
[18] E. A. Widder, *Science* **2010**, *328*, 704.
[19] D. E. McCoy, T. Feo, T. A. Harvey, R. O. Prum, *Nat. Commun.* **2018**, *9*, 1.
[20] T. Stegmaier, M. Linke, H. Planck, *Philos. Trans. R. Soc., A* **2009**, *367*, 1749.
[21] M. Spinner, A. Kovalev, S. N. Gorb, G. Westhoff, *Sci. Rep.* **2013**, *3*, 1846.
[22] P. Tao, W. Shang, C. Song, Q. Shen, F. Zhang, Z. Luo, N. Yi, D. Zhang, T. Deng, *Adv. Mater.* **2015**, *27*, 428.
[23] H. Lin, X. Wang, L. Yu, Y. Chen, J. Shi, *Nano Lett.* **2017**, *17*, 384.
[24] M. Alhabeb, K. Maleski, B. Anasori, P. Lelyukh, L. Clark, S. Sin, Y. Gogotsi, *Chem. Mater.* **2017**, *29*, 7633.
[25] A. Sarycheva, T. Makaryan, K. Maleski, E. Satheeshkumar, A. Melikyan, H. Minassian, M. Yoshimura, Y. Gogotsi, *J. Phys. Chem. C* **2017**, *121*, 19983.
[26] T.-H. Chang, T. Zhang, H. Yang, K. Li, Y. Tian, J. Y. Lee, P.-Y. Chen, *ACS Nano* **2018**, *12*, 8048.
[27] O. Mashtalir, M. Naguib, B. Dyatkin, Y. Gogotsi, M. W. Barsoum, *Mater. Chem. Phys.* **2013**, *139*, 147.
[28] Z. Y. Huang, W. Hong, Z. Suo, *J. Mech. Phys. Solids* **2005**, *53*, 2101.
[29] W. F. Hosford, *Mechanical Behavior of Materials*, Cambridge University Press, Cambridge **2010**.
[30] L. W. McKeen, in *Effect of Temperature and other Factors on Plastics and Elastomers*, 2nd ed. (Ed: L. W. McKeen), William Andrew Publishing, Norwich, NY **2008**, p. 41.
[31] A. Lipatov, H. Lu, M. Alhabeb, B. Anasori, A. Gruverman, Y. Gogotsi, A. Sinitskii, *Sci. Adv.* **2018**, *4*, eaat0491.
[32] Z. Ling, C. E. Ren, M.-Q. Zhao, J. Yang, J. M. Giammarco, J. Qiu, M. W. Barsoum, Y. Gogotsi, *Proc. Natl. Acad. Sci. U S A* **2014**, *111*, 16676.
[33] G. Berdiyorov, *AIP Adv.* **2016**, *6*, 055105.
[34] S. Zeng, D. Zhang, W. Huang, Z. Wang, S. G. Freire, X. Yu, A. T. Smith, E. Y. Huang, H. Nguon, L. Sun, *Nat. Commun.* **2016**, *7*, 11802.

[35] L. Zhou, Y. Tan, D. Ji, B. Zhu, P. Zhang, J. Xu, Q. Gan, Z. Yu, J. Zhu, *Sci. Adv.* **2016**, *2*, e1501227.

[36] M. D. Kelzenberg, S. W. Boettcher, J. A. Petykiewicz, D. B. Turner-Evans, M. C. Putnam, E. L. Warren, J. M. Spurgeon, R. M. Briggs, N. S. Lewis, H. A. Atwater, *Nat. Mater.* **2010**, *9*, 239.

[37] K. Chaudhuri, M. Alhabeb, Z. Wang, V. M. Shalaev, Y. Gogotsi, A. Boltasseva, *ACS Photonics* **2018**, *5*, 1115.

[38] B. Desiatov, I. Goykhman, U. Levy, *Nano Lett.* **2014**, *14*, 648.

[39] M. Acerce, D. Voiry, M. Chhowalla, *Nat. Nanotechnol.* **2015**, *10*, 313.

[40] L. Zhou, Y. Tan, J. Wang, W. Xu, Y. Yuan, W. Cai, S. Zhu, J. Zhu, *Nat. Photonics* **2016**, *10*, 393.

[41] O. Neumann, C. Feronti, A. D. Neumann, A. Dong, K. Schell, B. Lu, E. Kim, M. Quinn, S. Thompson, N. Grady, P. Nordlander, M. Oden, N. J. Halas, *Proc. Natl. Acad. Sci. U S A* **2013**, *110*, 11677.

[42] O. Neumann, A. S. Urban, J. Day, S. Lal, P. Nordlander, N. J. Halas, *ACS Nano* **2013**, *7*, 42.

[43] W. Shang, T. Deng, *Nat. Energy* **2016**, *1*, 16133.

[44] M. Zhu, Y. Li, F. Chen, X. Zhu, J. Dai, Y. Li, Z. Yang, X. Yan, J. Song, Y. Wang, E. Hitz, W. Luo, M. Lu, B. Yang, L. Hu, *Adv. Energy Mater.* **2018**, *8*, 1701028.

[45] X. Li, W. Xu, M. Tang, L. Zhou, B. Zhu, S. Zhu, J. Zhu, *Proc. Natl. Acad. Sci. U S A* **2016**, *113*, 13953.

[46] M. Ye, J. Jia, Z. Wu, C. Qian, R. Chen, P. G. O'Brien, W. Sun, Y. Dong, G. A. Ozin, *Adv. Energy Mater.* **2017**, *7*, 1601811.

[47] J. Wang, Y. Li, L. Deng, N. Wei, Y. Weng, S. Dong, D. Qi, J. Qiu, X. Chen, T. Wu, *Adv. Mater.* **2017**, *29*, 1603730.

[48] J. Yang, Y. Pang, W. Huang, S. K. Shaw, J. Schiffbauer, M. A. Pillers, X. Mu, S. Luo, T. Zhang, Y. Huang, G. Li, S. Ptasinska, M. Lieberman, T. Luo, *ACS Nano* **2017**, *11*, 5510.

[49] G. Wang, Y. Fu, X. Ma, W. Pi, D. Liu, X. Wang, *Carbon* **2017**, *114*, 117.

[50] Y. Li, T. Gao, Z. Yang, C. Chen, W. Luo, J. Song, E. Hitz, C. Jia, Y. Zhou, B. Liu, B. Yang, L. Hu, *Adv. Mater.* **2017**, *29*, 1700981.

[51] P. Mu, Z. Zhang, W. Bai, J. He, H. Sun, Z. Zhu, W. Liang, A. Li, *Adv. Energy Mater.* **2019**, *9*, 1802158.

[52] W. Xu, X. Hu, S. Zhuang, Y. Wang, X. Li, L. Zhou, S. Zhu, J. Zhu, *Adv. Energy Mater.* **2018**, *8*, 1702884.

[53] S. Hong, H. Lee, J. Lee, J. Kwon, S. Han, Y. D. Suh, H. Cho, J. Shin, J. Yeo, S. H. Ko, *Adv. Mater.* **2015**, *27*, 4744.

[54] S. Choi, J. Park, W. Hyun, J. Kim, J. Kim, Y. B. Lee, C. Song, H. J. Hwang, J. H. Kim, T. Hyeon, D.-H. Kim, *ACS Nano* **2015**, *9*, 6626.

[55] P.-C. Hsu, X. Liu, C. Liu, X. Xie, H. R. Lee, A. J. Welch, T. Zhao, Y. Cui, *Nano Lett.* **2015**, *15*, 365.

[56] M. Zhang, C. Wang, X. Liang, Z. Yin, K. Xia, H. Wang, M. Jian, Y. Zhang, *Adv. Electron. Mater.* **2017**, *3*, 1700193.

[57] H. Fan, K. Li, Q. Li, C. Hou, Q. Zhang, Y. Li, W. Jin, H. Wang, *J. Mater. Chem. C* **2017**, *5*, 9778.

[58] Z. Wang, A. von dem Bussche, Y. Qiu, T. M. Valentin, K. Gion, A. B. Kane, R. H. Hurt, *Environ. Sci. Technol.* **2016**, *50*, 7208.

[59] H. Huang, Y. Cui, Q. Li, C. Dun, W. Zhou, W. Huang, L. Chen, C. A. Hewitt, D. L. Carroll, *Nano Energy* **2016**, *26*, 172.

[60] M. J. Shenton, M. C. Lovell-Hoare, G. C. Stevens, *J. Phys. D: Appl. Phys.* **2001**, *34*, 2754.

[61] T. Lin, C. Yang, Z. Wang, H. Yin, X. Lü, F. Huang, J. Lin, X. Xie, M. Jiang, *Energy Environ. Sci.* **2014**, *7*, 967.

1901687 (14 of 14)